CHEMISTRY OF MATERIALS
Cite This: Chem. Mater. 2019, 31, 3183−3191
Article
pubs.acs.org/cm

Tuning Anionic Chemistry To Improve Kinetics of Mg Intercalation

Minglei Mao,[†,‡,§] Xiao Ji,[†,§] Singyuk Hou,[†] Tao Gao,[†] Fei Wang,[†] Long Chen,[†] Xiulin Fan,[†] Ji Chen,[†] Jianmin Ma,[‡] and Chunsheng Wang*[,†]

[†]Department of Chemical and Biomolecular Engineering, University of Maryland, College Park, Maryland 20742, United States
[‡]State Key Laboratory of Chemo/Biosensing and Chemometrics, School of Physics and Electronics, Hunan University, Changsha 410082, China

Supporting Information

ABSTRACT: Rechargeable Mg batteries (RMBs) hold great promise for high energy density in consumer electronics because of the high theoretical volumetric capacity and dendrite-free stripping/plating of Mg. Their development, however, is severely limited by the sluggish diffusion of Mg^{2+} in inorganic cathodes, mainly induced by strong interaction between Mg^{2+} and host anions. Herein, for the first time, we systematically investigate how anionic chemistry (O, S, and Se) affects Mg^{2+} migration in layered MX_2 (M = Ti and V; X = O, S, and Se), by combining theoretical density functional theory (DFT) calculations with electrochemical characterizations. At room temperature, $TiSe_2$ and VSe_2 achieve much better electrochemical performance than TiS_2 and VS_2, due to the faster migration of Mg^{2+} in selenide than in sulfide and oxide, as demonstrated by electrochemical kinetic characterizations and DFT calculations. The improved kinetics of selenide can be attributed to three criteria: (i) larger diffusion channel, (ii) weaker interaction between Mg^{2+} and anion lattice, and (iii) higher electronic conductivity. The three criteria might not only be applicable to layered materials but also be generalizable to materials with other structures, like Chevrel phase, spinel, olivine, etc., which paves the way for the future design and modification of intercalation materials for RMBs.

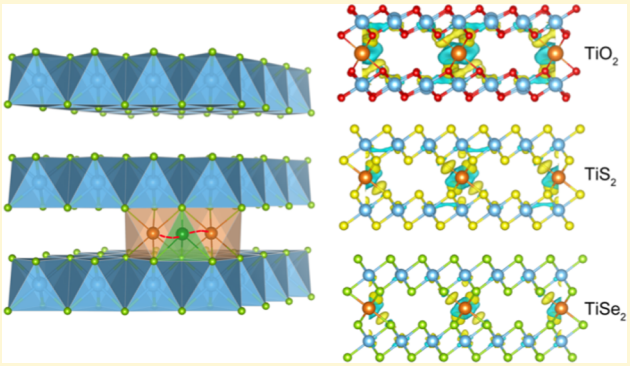

INTRODUCTION

With the increasing demand for green energy, lithium-ion batteries (LIBs) have dominated electric vehicles and consumer electronics.[1−3] However, as the energy density of LIBs reaches the limitation of intercalation chemistry, rechargeable metal batteries are becoming promising candidates owing to the high-capacity metal anodes.[4−6] Among them, rechargeable Mg batteries (RMBs) stand out, due to the merits of low potential (−2.37 V vs Mg/Mg^{2+}), high volumetric energy density (3800 Wh/cm^3), rich storage on earth, and, more importantly, highly reversible (close to 100% Coulombic efficiency (CE)) dendrite-free stripping/deposition of Mg in certain electrolytes.[7−9] Therefore, RMBs are becoming one of the most promising candidates for application in consumer electronics, in which volumetric energy density and safety are the priority.

In recent years, significant advances have been achieved in RMB electrolytes.[10−12] The development of RMBs, however, is severely limited by the lack of high-performance cathodes.[13,14] Inspired by the great success in LIBs, intercalation materials, especially layered materials, are drawing the most attention as cathodes for RMBs because of their chemical stability, high redox potentials, and reversibility.[15−18] However, layered cathodes for RMBs suffer sluggish migration of Mg^{2+} in solid hosts, due to the strong interaction between Mg^{2+} and anions of host structure.[19−23] According to previous research, the effect of transition metals on the migration of Mg is very weak,[19,20,24] while the strong interaction between anions and Mg^{2+} is the major contribution to the sluggish kinetics.[19,20,25−28] Recent findings demonstrate that oxide cathode materials exhibit extremely sluggish kinetics,[20,29,30] while soft anions (S and Se) have high Mg^{2+} mobility.[19,31,32] The mechanism is not fully understood. A deep understanding of how anionic chemistry affects Mg^{2+} migration in layered materials would be of paramount significance for the future design of RMB cathode materials.

Herein, for the first time, we systematically investigated how different anionic chemistry (O, S, and Se) affects Mg^{2+} migration in layered MX_2 (M = Ti, V; X = O, S, Se), by combining theoretical calculations with electrochemical characterizations. Three kinetics criteria were proposed based on the correlation between anionic chemistry and intercalation kinetics in layered materials, which might be generalizable to other types of intercalation cathode materials. This work can provide the basis for electrode material design and pave the

Received: December 18, 2018
Revised: April 12, 2019
Published: April 15, 2019

DOI: 10.1021/acs.chemmater.8b05218
Chem. Mater. 2019, 31, 3183−3191

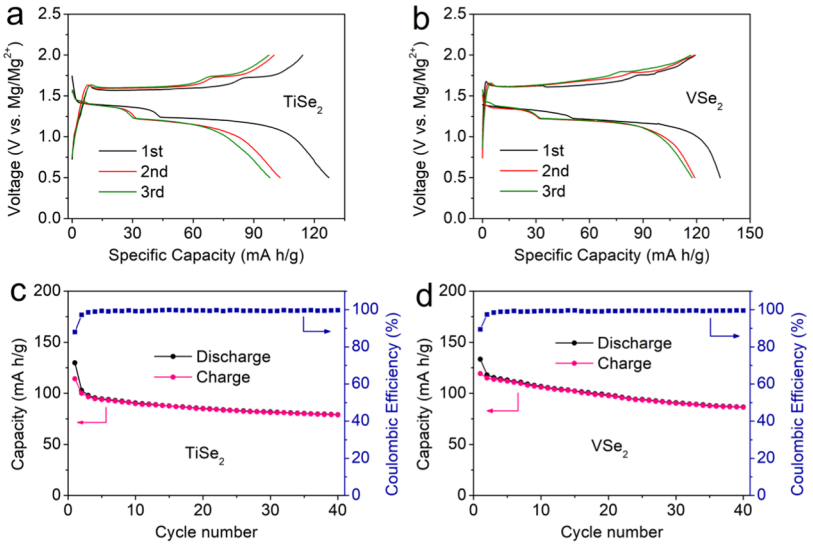

Figure 1. Discharge−charge curves of (a) $TiSe_2$ and (b) VSe_2 for the first three cycles. Cycling performance and Coulombic efficiency (CE) of (c) $TiSe_2$ and (d) VSe_2 with APC electrolyte and metal Mg anode between 0.5 and 2 V at a current density of 5 mA/g under room temperature.

way for exploring intercalation materials with fast kinetics for RMBs.

RESULTS AND DISCUSSION

Electrochemical Performance of MX_2. MX_2 (M = Ti, V; X = O, S, Se) with $P\bar{3}m1$ structure are selected as model cathodes to investigate the impact of anionic chemistry on Mg^{2+} migration kinetics, because they are representative and mostly investigated layered cathodes for RMBs.[8,13,31,33] Density functional theory calculations demonstrate that TiS_2, $TiSe_2$, and VSe_2 are thermodynamically stable, while VS_2 is metastable exhibiting moderate energy above hull values of 20 meV/atom. Although common TiO_2 (anatase, brookite, and rutile)[34] and VO_2 (rutile)[35] are stable at room temperature (RT), layered VO_2 and TiO_2 with $P\bar{3}m1$ structure fall into the unstable range with large energy above hull (>85 meV/atom). Therefore, the discussion about the oxides only limits to calculation.

Based on the thermodynamic stability of MX_2 compounds, TiS_2, $TiSe_2$, and VSe_2 were synthesized by solid-state reaction with VS_2 by the hydrothermal method. As confirmed by X-ray diffraction (XRD) (Figure S1), all of the patterns of these compounds were indexed in the standard $P\bar{3}m1$ space group, consistent with previous reports.[36−39] As the particle sizes determine the diffusion length of Mg^{2+}, we managed to synthesize the particles of these compounds with a similar size (1−20 μm), which is also confirmed by scanning electron microscopy (SEM) (Figure S2). Thus, the difference in electrochemical performance between these isostructure materials can be only attributed to their difference in anionic chemistry.

Electrochemical performance of TiS_2, $TiSe_2$, VS_2, and VSe_2 cathodes was examined with excess Mg metal as the anode in all phenyl complex (APC) electrolyte between 0.5 and 2 V, using 2032 coin cells at room temperature. Figures 1a,b and S3a,b show the discharge/charge curve for the first three cycles at a current density of 5 mA/g. For sulfide, TiS_2 and VS_2 deliver the negligible capacities (less than 10 mA h/g) with low Coulombic efficiency (CE) (Figure S3a,b), indicating the high migration barriers and Mg^{2+} trapped in TiS_2 and VS_2.[25] In contrast, much higher capacities with a low overpotential and high CE are achieved for $TiSe_2$ and VSe_2 (Figure 1a,b). $TiSe_2$ delivers the first discharge capacity of 127 mA h/g (close to its theoretical capacity: 130 mA h/g) with two plateaus at 1.35−1.4 and 1.15−1.24 V, and 114 mA h/g can be recovered on charge with two plateaus at 1.73−1.75 and 1.57−1.58 V, corresponding to the CE of 89.7%. Similarly, VSe_2 (theoretical capacity: 128 mA h/g) can render a reversible capacity of 115 mA h/g after the first three cycles, with two plateaus on both discharge and charge, indicating similar intercalation and deintercalation processes between $TiSe_2$ and VSe_2.

In addition, two plateaus on the discharge and charge processes in $TiSe_2$ and VSe_2 indicate two steps for Mg^{2+} intercalation into interlayers of $TiSe_2$ and VSe_2, which are related to the different vacancy location of Mg^{2+} (tetrahedral or octahedral sites).[38,40] The flat voltage plateaus indicate a two-phase region, induced by the formation of distortion in $TiSe_2$ and VSe_2 hosts.[41] The distortion is a consequence of changing the ionic character of the bond via magnesium intercalation and electron donation to the host.[42,43]

The phase change due to distortion in $TiSe_2$ and VSe_2 hosts was also investigated using cyclic voltammetry at a sweep rate of 0.2 mV/s between 0.5 and 2 V (Figure S4). Both $TiSe_2$ and VSe_2 exhibit two cathodic peaks during discharge but only one anodic peak during charge. Two cathodic peaks correspond to two voltage plateaus in discharge curves (Figure 1a,b), whereas two voltage plateaus merge into one peak during charge due to the closed voltages. At the same sweep rate, the current at cathodic and anodic peaks for selenide is higher than that for sulfide (Figure S4), indicating the fast intercalation reaction kinetics.[44]

Cycling stability of TiS_2, $TiSe_2$, VS_2, and VSe_2 was evaluated in coin cells with APC electrolyte and an excess Mg negative electrode at 5 mA/g and room temperature (RT) (Figures 1c,d and S3c,d). TiS_2 and VS_2 deliver a low capacity of less than 10 mA h/g (Figure S3c,d). In contrast, $TiSe_2$ and VSe_2 maintain capacities of 80 and 86 mA h/g after 40 cycles, with the Coulombic efficiencies (CEs) above 99.3 and 99.5%, respectively (Figure 1c,d). The slight capacity decay may be associated with the minor dissolution of layered $TiSe_2$ and VSe_2 into electrolytes.

DOI: 10.1021/acs.chemmater.8b05218
Chem. Mater. 2019, 31, 3183−3191

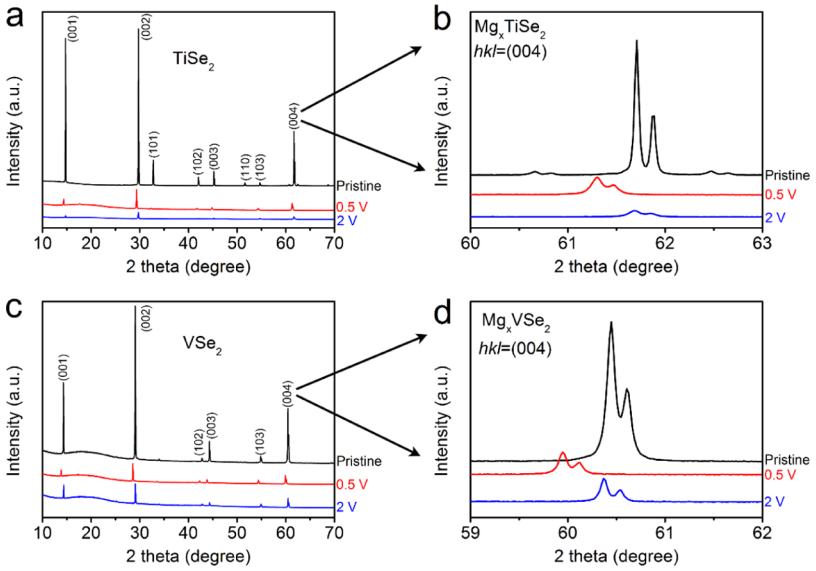

Figure 2. Ex situ XRD of (a) $TiSe_2$ and (c) VSe_2 for pristine (black), discharged to 0.5 V (red) and charged to 2 V (blue) for the first cycle, respectively. (004) peak shift of (b) $TiSe_2$ and (d) VSe_2 during discharging and charging processes, respectively.

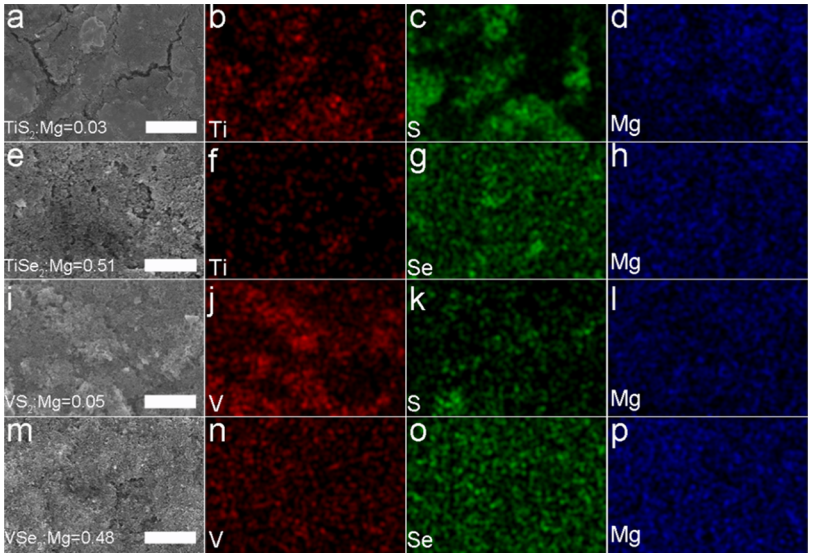

Figure 3. Morphologies and energy-dispersive spectroscopy (EDS) elemental mapping of discharged (a–d) TiS_2, (e–h) $TiSe_2$, (i–l) VS_2, and (m–p) VSe_2. The scale bars in (a), (e), (i), and (m) represent 2 μm. All of the samples are discharged to 0.5 V.

Mg^{2+} Diffusion-Controlled MX_2 Cathodes. The reversible intercalation of Mg^{2+} into selenide is confirmed by XRD (Figure 2) and energy-dispersive spectroscopy (EDS, Figure 3). The $P\bar{3}m1$ layered structure of $TiSe_2$ and VSe_2 maintains after the first discharge and charge processes (Figure 2a,c). During discharge, peaks of XRD shift to the lower angles, indicating that Mg^{2+} is intercalated into the layers of $TiSe_2$ and VSe_2 (Figure 2b,d). On charge, the peaks shift back to an initial angle but without overlapping the initial peaks, indicating the incomplete deintercalation of Mg^{2+} from $TiSe_2$ and VSe_2 with some Mg^{2+} trapped. EDS was applied to quantify Mg^{2+} intercalation into sulfide and selenide (Figure 3). After discharging to 0.5 V, the amount of Mg^{2+} intercalated into selenide (0.51 Mg/$TiSe_2$ and 0.48 Mg/VSe_2) is much higher than the amount of Mg^{2+} intercalated into sulfide (0.03 Mg/TiS_2 and 0.05 Mg/VS_2), which is consistent with the discharge capacities.

The overpotential and quasi-equilibrium potential of TiS_2, $TiSe_2$, VS_2, and VSe_2 during discharge and charge were collected using galvanostatic intermittent titration technique (GITT) (Figures 4a,b and S5). The cells were allowed to relax at the open circuit for 5 h to reach quasi-equilibrium, after each 2 h discharging or charging at 5 mA/g in the first cycle (Figures 4a,b and S5). GITT can provide information on both thermodynamic hysteresis and kinetic polarization.[45,46] The cumulative capacities of these four compounds are slightly higher than their capacities during the galvanostatic process due to the relaxation process in each discharge/charge process. Apparently, the overpotentials for TiS_2 and VS_2 (Figure S5) are much higher than those for $TiSe_2$ and VSe_2 (Figure 4a,b), respectively, especially during discharging process, indicating the faster kinetics for Mg^{2+} diffusion in selenide. The quasi-equilibrium potentials for TiS_2 and VS_2 are higher than those for $TiSe_2$ and VSe_2, respectively, due to the stronger

DOI: 10.1021/acs.chemmater.8b05218
Chem. Mater. 2019, 31, 3183–3191

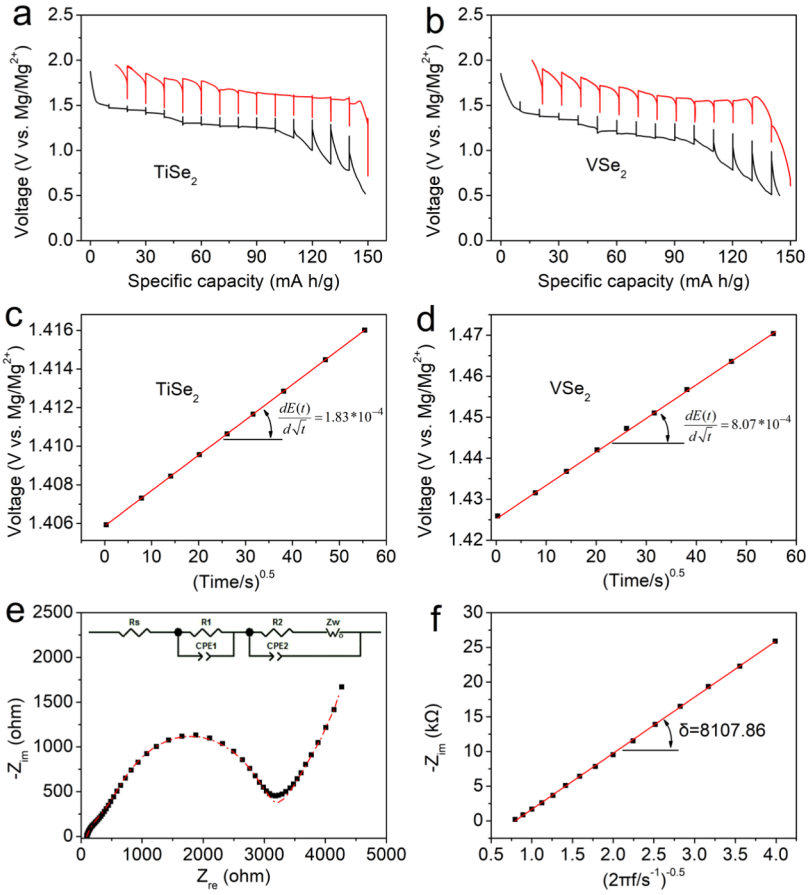

Figure 4. Quasi-equilibrium voltage profile of (a) $TiSe_2$ and (b) VSe_2 obtained from GITT. The cells were allowed to relax for 5 h after every 2 h discharging or charging at 5 mA/g at RT. Representation of the transient voltage of galvanostatic pulse as a function of the square root of time from GITT for (c) $TiSe_2$ and (d) VSe_2. (e) Nyquist plots for $TiSe_2$ cells at open-circuit voltage states obtained by electrochemical impedance spectroscopy (EIS) tests. The red dashed lines are the fitting curve by using the equivalent circuit, which consists of a resistor (R_s), a resistor (R_1) paralleled with a constant phase element (CPE), and a CPE parallel with a resistor (R_2). (f) Plot of the imaginary resistance versus the inverse square root of angular frequency from EIS for $TiSe_2$. The red dashed line corresponds to the linear fitting with the slope marked out.

interaction between Mg^{2+} and sulfide host, which will be discussed below.

The chemical diffusion coefficient for Mg^{2+} in TiS_2, $TiSe_2$, VS_2, and VSe_2 at different charge/discharge states can be obtained from GITT using eq I[44,47]

$$D = \frac{4}{\pi}\left(\frac{IV_M}{Z_A FS}\right)^2\left[\frac{dE(x)}{dx}\Big/\frac{dE(t)}{d\sqrt{t}}\right]^2 \quad \text{(I)}$$

where I is the applied constant current, V_M is the molar volume (112 cm^3/mol for TiS_2, 205.79 cm^3/mol for $TiSe_2$, 115.07 cm^3/mol for VS_2, and 208.86 cm^3/mol for VSe_2), assumed to be constant during the electrochemical process, Z_A is the charge number of electroactive species Mg^{2+}, F is the Faraday constant (96 486 C/mol), S is the electrochemically active area between the electrode material and electrolyte from Brunauer–Emmett–Teller surface area (4585.32 cm^2/g for TiS_2, 5706.68 cm^2/g for $TiSe_2$, 16238.16 cm^2/g for VS_2, and 4301.45 cm^2/g for VSe_2), $E(x)$ is the equilibrium voltage (i.e., open-circuit voltage) of the working electrode (vs reference electrode) at the composition of Mg_xTiS_2, and $E(t)$ is the transient voltage response of the working electrode during the constant current interval.

The transient voltage versus the square root of the time of $TiSe_2$ and VSe_2 is plotted in Figure 4c,d, respectively. Plugging the slope of the linear fitting into eq I, we can get the diffusion coefficient of Mg^{2+} in $TiSe_2$ and VSe_2 to be 9.65×10^{-20} and 6.17×10^{-20} cm^2/s, respectively. In contrast, the diffusion coefficients in VS_2 and TiS_2 are 1.04×10^{-23} and 4.20×10^{-23} cm^2/s, respectively. The diffusion coefficient of selenide is 3 orders of magnitude higher than that of sulfide, indicating the faster migration of Mg^{2+} in selenide.

Mg^{2+} diffusion coefficient obtained from GITT was also cross-checked using eq II from electrochemical impedance spectroscopy (EIS)

$$D = \frac{1}{2}\left[\left(\frac{V_M}{AF\delta}\right)\left(\frac{dE}{dx}\right)\right]^2 \quad \text{(II)}$$

where δ is the slope of the Warburg straight line (Ω/s), A (cm^2) is the effective contact area between the electrolyte and electrode materials, which can be obtained by multiplying S in eq I by the loading amount of active materials, and other symbols have the same meaning as they have in eq I.

The impedance data are fitted with the equivalent circuit shown in the inset of Figure 4e. The resistor R_s corresponds to the electrolyte resistance. The resistors R_1 and R_2 paralleled with the constant phase element (CPE) account for the surface reaction resistance of both $TiSe_2$ cathode and Mg anode. The ion diffusion in the host material is described as the Warburg element (Z_w) in low frequency. The simulated data from the

DOI: 10.1021/acs.chemmater.8b05218
Chem. Mater. 2019, 31, 3183–3191

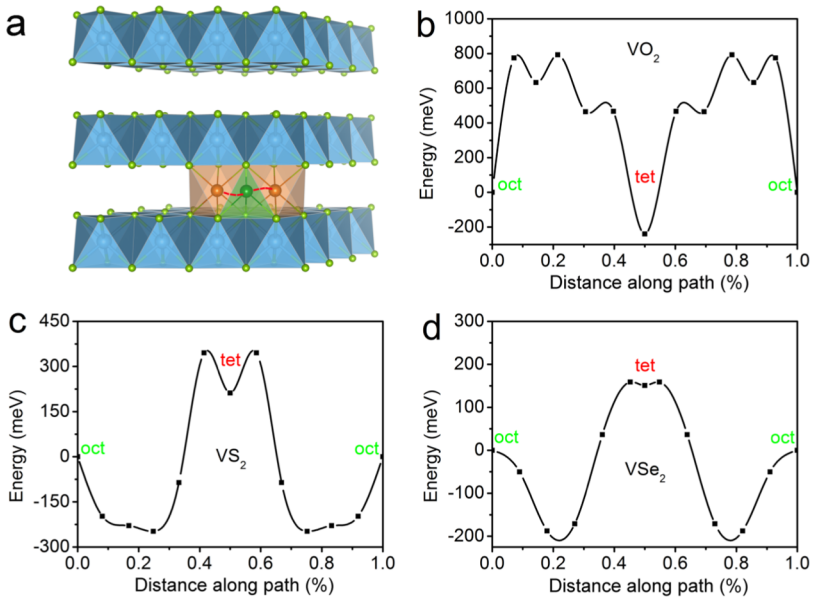

Figure 5. (a) Crystal structure of layered MX_2 (M = Ti, V; X = O, S, Se). Ti or V atoms (blue) are at the center of octahedra constructed of X atoms (green). Mg^{2+} migrates between the empty interlayer octahedral sites (orange) through the intermediate tetrahedral sites (olivine), which is marked in red dashed line. Calculated energy barrier for the migration of Mg^{2+} in layered structure along the minimum energy path as obtained by first-principles nudged elastic band (NEB) in calculations. (b) VO_2, (c) VS_2, and (d) VSe_2 within the dilute limit of cation insertion.

equivalent circuit well fit the impedance data for layered $TiSe_2$ at open-circuit voltage states (Figure 4e). Figure 4f shows the plot of the imaginary resistance determined by EIS as a function of the inverse square root of the angular frequency for $TiSe_2$. Plugging the slope of the linear fitting into eq II, the diffusion coefficient for $TiSe_2$ is 4.85×10^{-19} cm^2/s. Applying the same method, the diffusion coefficients for TiS_2, VS_2, and VSe_2 are 3.10×10^{-22}, 3.20×10^{-22}, and 6.73×10^{-19} cm^2/s, respectively. The Mg^{2+} diffusion coefficient for Ti or V sulfides and selenides obtained by the direct modeling of the EIS measurements is slightly higher than that determined by GITT, which has been reported in other cathodes.[25,48] From both GITT and EIS measurements, the chemical diffusion coefficient for Mg^{2+} in Ti or V selenide are ~3 orders of magnitude higher than that in sulfide.

CV is an efficient tool to investigate the charge-storage kinetics of electrodes. In theory, the peak current (i) at a fixed potential obeys a power law relationship with the sweep rate (v)[49]

$$i = av^b$$

The value of b can be calculated from the slope of $\log(v)-\log(i)$ plots. A b-value of 0.5 indicates that the related electrochemical process is totally diffusion-controlled,[50] while $b = 1$ means a complete adsorption-controlled behavior, corresponding to a capacitor-like process.[51,52] As shown in Figure S6a, all of the curves exhibit similar shapes for both cathodic and anodic processes at different sweep rates in the range of 0.1−1 mV/s. The $\log(i)$ versus $\log(v)$ plot for the anodic peak at ~1.8 V (versus Mg/Mg^{2+}) shows that the b-values for $TiSe_2$ and VSe_2 are 0.58 and 0.57 (Figure S6b), respectively, indicating that the charge storage is mainly controlled by diffusion processes.

Mg^{2+} Diffusion Mechanism in MX_2. To reveal the mechanism behind the drastic difference among layered oxide, sulfide, and selenide in electrochemical performance and diffusion coefficient, nudged elastic band (NEB) calculations were performed to compute the diffusion activation barriers along the migration path for layered MX_2 (M = Ti, V; X = O, S, Se) in the limit of dilute Mg^{2+} insertion. Layered MX_2 ($P\bar{3}m1$) consists of stacking sequences of the MX_2 slabs, each of which is composed of stacking of close-packed two-dimensional triangular lattices of X (Figure 5a). The M atoms occupy octahedrally (tetrahedrally for oxides) coordinated interstitial sites between the X planes. Mg^{2+} diffuses between the stable octahedral sites (tetrahedral sites for oxides) through intermediate tetrahedral sites (octahedral sites for oxides), where the energy exhibits a local minimum before moving to the adjacent octahedral sites (Figures 5a and S7). The migration for Mg^{2+} in layered VO_2 and VS_2 exhibits the activation barriers of 1032 and 593 meV (Figure 5b,c), respectively, which are too high for Mg^{2+} diffusion at room temperature (RT),[20] whereas VSe_2 displays the lowest activation barrier of 346 meV (Figure 5d), affording the Mg^{2+} migration at RT. The different profile of oxides from sulfides and selenides is related to the unstable layered structure, while the positions of energetic minima located at ~0.2 and ~0.8 of the diffusion path are due to some distortion of the layered structure during Mg^{2+} diffusion. Similarly, the migration energy barrier for $TiSe_2$ is also lower than that for TiS_2 (Figure S8). In addition to oxide, sulfide, and selenide, we also extend our experiments and calculations to telluride (Figure S9). Layered $TiTe_2$ is prepared with the solid-state method (Figure S9a) and delivers a capacity of ~86 mA h/g (close to its theoretical capacity of 88 mA h/g) during the first three cycles with lower overpotential than $TiSe_2$ (Figure S9b). In addition, the energy barrier for the migration of Mg^{2+} in $TiTe_2$ is calculated to be lower than that of $TiSe_2$ (Figure S9c), indicating the better diffusion kinetics of Mg^{2+} in $TiTe_2$.

The trend for decreasing migration barriers in the series of "oxide−sulfide−selenide" compounds with the same structure mainly results from the different anionic chemistry in electronegativity (O > S > Se) and ionic radii (O^{2-} (1.32 Å) < S^{2-} (1.82 Å) < Se^{2-} (1.93 Å)).[53] In MX_2 (M = Ti, V; X = O,

DOI: 10.1021/acs.chemmater.8b05218
Chem. Mater. 2019, 31, 3183−3191

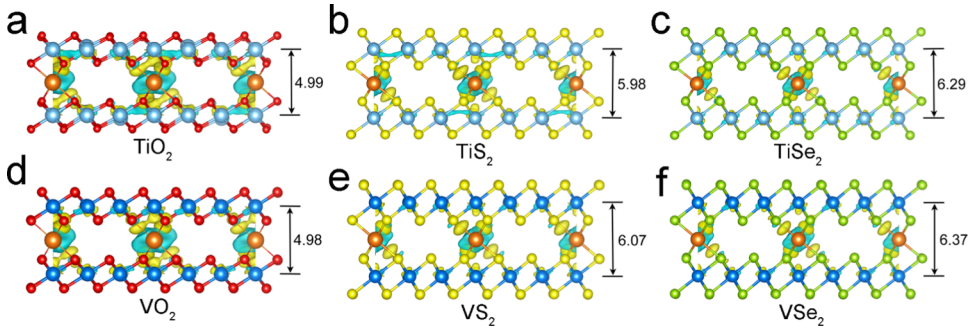

Figure 6. Charge rehybridization upon the diffusion of Mg^{2+} between layers of (a) TiO_2, (b) TiS_2, (c) $TiSe_2$, (d) VO_2, (e) VS_2, and (f) VSe_2 with layer spacing (unit/Å). Areas of charge accumulation are shown in yellow, while depletion is shown in blue. Oxygen atoms are shown as small red spheres, sulfur as small yellow spheres, selenium as small kelly spheres, Ti as large sapphire spheres, V as big green spheres, and Mg at the center as an orange sphere. The isovalue number used for displaying the differential charge density is 0.003.

S, Se), Mg^{2+} diffuses between layers from the stable octahedral sites, crossing through a three-coordinated oxygen (sulfur or selenium) face into the intermediate tetrahedral site and finally to the next stable octahedral site through a symmetric path. The size of Mg^{2+} diffusion channel is dictated by the space between layers. From TiO_2 (VO_2) to $TiSe_2$ (VSe_2), the spacing between layers increases from 4.99 (4.98) to 6.29 Å (6.37 Å) (Figure 6), indicating the increasing size of diffusion channel, affording faster Mg^{2+} mobility in selenide than that in sulfide and oxide.

The activation energy of Mg^{2+} motion depends on, in particular, the deformability of the electron clouds of the anionic framework.[25] The high deformability will easily accommodate the charge brought by intercalated Mg^{2+}, which contributes to Mg^{2+} mobility. When Mg^{2+} is intercalated, electrons accompanying Mg^{2+} are donated to the host. The increased negative charge around the Ti or V ions, in turn, raises the energy of d states relative to that of the X p states, which will increase the ionic character of the M−X bonds (M = Ti, V; X = O, S, Se) due to a reduction in the hybridization between M d states and X p states. Figure 6 shows the charge rehybridization upon the diffusion of Mg^{2+} between layers of MX_2. These charge difference plots were obtained by subtracting the charge densities of both MX_2 structures and an isolated Mg atom from the charge density of Mg_yMX_2. The charge difference plots therefore show how charge redistributes upon the addition of Mg to MX_2. Yellow color signifies an accumulation, while blue signifies a depletion of electron density. As Mg^{2+} migrates through the layers of MX_2, it will drag the electron cloud residing on the coordinating X anions with it. The surrounding M and X ions will therefore be required to rehybridize as the cation moves. While TiX_2 (or VX_2) hosts consist of the same $P\bar{3}m1$ structure, the different degree of rehybridization results from the different anionic chemistry (O, S, and Se). The higher the degree of rehybridization, the lower the deformability.[25] Obviously, the charge rehybridization for layered TiX_2 (or VX_2) decreases in the series of "O−S−Se", indicating the increasing deformability in this series, which accounts for the lowest diffusion barriers in $TiSe_2$ and VSe_2.

The electronic conductivity of the host is another important parameter that determines the mobility of Mg^{2+}. It is proposed that intercalation diffusion rates are dependent on the ease with which the electron cloud in the host can travel through the lattice to accompany the moving cation, which has been demonstrated by Mg^{2+}-intercalated Mo_6S_8.[54] With the metallic electronic structure, the ionic charges of Mo_6S_8 anions are shielded from the highly charged Mg ion by the itinerant electrons of the framework, resulting in the easy migration of Mg^{2+} in the lattice. However, when the charge brought by Mg^{2+} satisfies the electronic configuration of S atoms and induces a metal-to-semiconductor transition of $Mg_2Mo_6S_8$, the mobility of Mg^{2+} within $Mg_2Mo_6S_8$ becomes poor. Density of states (DOS), as a major factor in the determination of the electronic conductivity of inorganic materials, was calculated by first-principle calculation (Figure S11). A wide energy gap is observed in the total DOS of layered TiO_2, indicating the nature of semiconductor (Figure S11a). While for $TiSe_2$ and VSe_2 (Figure S10c,f), the electronic states around the Fermi level (E_f) consist of both 3d orbital of Ti (V) and 4p orbital of Se, indicating that $TiSe_2$ and VSe_2 are metals with the Fermi energy line entered into the conduction band. In addition, the electronic conductivities of TiS_2, $TiSe_2$, VS_2, and VSe_2 were experimentally measured to be 1.04×10^5, 7.84×10^6, 4.57×10^6, and 9.60×10^6 S/m, respectively, which is consistent with the reported electronic conductivity order of selenide > sulfide > oxide.[55−58]

Based on the discussion above, the layered selenide displays the lowest Mg^{2+} migration barriers and the best electrochemical performance among layered MX_2 (M = Ti, V; X = O, S, Se), which can be summarized into three main factors:[19,20,54,59] (i) larger sizes of diffusion channel, due to the longer interlayer distance and Mg−Se bond; (ii) less strong interaction between Mg^{2+} and hosts, which can be demonstrated by less charge rehybridization upon Mg^{2+} diffusion between layers; (iii) higher electronic conductivity so that the electron cloud in the host can travel more easily through the lattice to accompany the moving Mg^{2+}.

The three criteria for fast Mg^{2+} migration kinetics developed from layered cathodes with a trigonal structure are also applicable to materials with monoclinic ($P2\bar{1}m$) and triclinic structures ($P\bar{1}$) (Figure S12). $NbSe_3$ shows much faster kinetics for Mg^{2+} intercalation and higher magnesiation level with a higher CE (Figure S13) than NbS_3 (Figure S14). More broadly, the reported electrochemical performance of cathodes with Chevrel phase,[25,27] spinel,[19,60] and olivine[61,62] structures also supports the three criteria. The high Mg^{2+} mobility can be achieved only when all three criteria are satisfied at the same time. For example, Chevrel phase (Mo_6S_8 or Mo_6Se_8) with large diffusion channel, weak interaction between Mg^{2+} and host lattice, and metallic electronic structure has been proven to be the most successful cathode for RMBs.[63,64] Sulfide spinel

DOI: 10.1021/acs.chemmater.8b05218
Chem. Mater. 2019, 31, 3183−3191

compounds have experimentally demonstrated to achieve high electrochemical performance,[19,60] while the corresponding oxide spinel compounds with smaller diffusion channel, stronger interaction between Mg^{2+} with host anions, and lower electronic conductivity have not been demonstrated with any electrochemical activity for Mg^{2+} storage.[20] Olivine $MgFeSiO_4$ is calculated with a lower migration barrier of 600 meV[65] and experimentally achieves high electrochemical performance,[62] whereas olivine $Mg_{0.5}FePO_4$ with a barrier of 1025 meV hardly intercalates any Mg^{2+},[66] due to the stronger interaction between Mg^{2+} with PO_4^{4-} than that with SiO_4^{4-}.

We want to emphasize that synergy among these three criteria is necessary to achieve high Mg^{2+} mobility, i.e., Mg^{2+} mobility would be too low to achieve high magnesiation level if any of these three criteria is not well satisfied. Besides the just mentioned oxide spinel compounds and olivine $Mg_{0.5}FePO_4$, layered MoS_2 with a large interlayer spacing of 6.2 Å and moderate interaction between Mg^{2+} and host anions delivers very low magnesiation degree because of its semiconductor electronic structure.[67,68] In other words, these three factors can explain most of the experimental findings in intercalation materials for RMBs. Accordingly, the effect of anionic chemistry on the kinetics of Mg^{2+} migration in intercalation compounds might apply to materials not only with a trigonal structure but also with monoclinic and triclinic structures, as well as reported Chevrel phase, spinel, and olivine.

In addition to different structures, the above discussion shows that the three criteria could be extended from chalcogen anions (oxide, sulfide, and selenide) to other anions, like halogen anions (fluoride, chloride, and bromide), hydroxyl, and polyanion. For example, polyanionic compounds might provide good mobility because of a more covalent bonding framework with weaker electrostatic interactions between Mg^{2+} and the host.[69] Also, some Prussian blue analogues have been demonstrated to intercalate Mg^{2+} reversibly[70] and benefit from large voids in the open framework structure and weak interaction of Mg^{2+} with the framework constituents.

The three criteria can also provide the following material design principle or modification measures to potentially improve the magnesiation kinetics of intercalation compounds: (i) replacing anion species with less electronegative ones and (ii) incorporating monovalent anions to reduce the electrostatic interaction between intercalant and host and improve the intercalated Mg^{2+} mobility. For example, theoretical calculations predict that partially substituting the O atom with F in one corner of "transition-metal-oxygen" octahedron increases the Mg ion mobility for both VPO_4F and $FeSO_4F$.[13,71] In addition, (iii) combining mixed transition-metal ions in oxides with an open-tunnel structure might contribute to charge redistribution and electronic conductivity,[72] which helps in the Mg^{2+} intercalation.

CONCLUSIONS

In this paper, we systematically studied how anionic chemistry affects Mg intercalation kinetics using layered MX_2 (M = Ti, V; X = O, S, Se) structure as an example system. The mechanism for higher electrochemical performance and lower migration barriers of selenide than sulfide and oxide was revealed by the correlation between anionic chemistry and intercalation kinetics. Three kinetics criteria are proposed to contribute to the better kinetics of layered selenide: (i) larger sizes of diffusion channel; (ii) less strong interaction between Mg^{2+} and host anions; and (iii) higher electronic conductivity. The criteria derived from layered materials might be generalized to other intercalation compounds, including Chevrel phase, spinel, olivine, etc. This systematic study will provide direction and standard for selecting and designing high-performance cathodes with fast kinetics for RMBs.

ASSOCIATED CONTENT

Supporting Information

The Supporting Information is available free of charge on the ACS Publications website at DOI: 10.1021/acs.chemmater.8b05218.

Experimental details, XRD and SEM of pristine MX_2, electrochemical characterizations, calculated energy barriers for the migration of Mg in TiS_2 and $TiSe_2$, DOS of MX_2, and electrochemical performance of $NbSe_3$ and NbS_3 (PDF)

AUTHOR INFORMATION

Corresponding Author

*E-mail: cswang@umd.edu.

ORCID

Tao Gao: 0000-0003-0204-3269

Xiulin Fan: 0000-0001-7294-480X

Ji Chen: 0000-0003-0326-8304

Chunsheng Wang: 0000-0002-8626-6381

Author Contributions

§M.M. and X.J. contributed equally to this work.

Notes

The authors declare no competing financial interest.

ACKNOWLEDGMENTS

The authors acknowledge the support from the Nanostructures for Electrical Energy Storage (NEES), an Energy Frontier Research Center funded by the US Department of Energy, Office of Science, Basic Energy Sciences, under Award Number DESC0001160. This work was also supported by the National Natural Science Foundation of China (Grant No. 51302079) and the Hunan Provincial Innovation Foundation for Postgraduate (No. CX2016B120). M.M.'s fellowship was supported by the China Scholarship Council (Grant No. 201606130050).

REFERENCES

(1) Scrosati, B. Battery Technology. *Nature* **1995**, *373*, 557−558.

(2) Armand, M.; Tarascon, J. M. Building better batteries. *Nature* **2008**, *451*, 652−657.

(3) Tarascon, J.-M.; Armand, M. Issues and challenges facing rechargeable lithium batteries. *Mater. Sustainable Energy* **2012**, 171−179.

(4) Whittingham, M. S. Ultimate Limits to Intercalation Reactions for Lithium Batteries. *Chem. Rev.* **2014**, *114*, 11414−11443.

(5) Scrosati, B. Recent advances in lithium ion battery materials. *Electrochim. Acta* **2000**, *45*, 2461−2466.

(6) Yoo, H. D.; Shterenberg, I.; Gofer, Y.; Gershinsky, G.; Pour, N.; Aurbach, D. Mg rechargeable batteries: an on-going challenge. *Energy Environ. Sci.* **2013**, *6*, 2265−2279.

(7) Muldoon, J.; Bucur, C. B.; Gregory, T. Quest for Nonaqueous Multivalent Secondary Batteries: Magnesium and Beyond. *Chem. Rev.* **2014**, *114*, 11683−11720.

(8) Canepa, P.; Sai Gautam, G.; Hannah, D. C.; Malik, R.; Liu, M.; Gallagher, K. G.; Persson, K. A.; Ceder, G. Odyssey of Multivalent Cathode Materials: Open Questions and Future Challenges. *Chem. Rev.* **2017**, *117*, 4287−4341.

(9) Gao, T.; Hou, S.; Huynh, K.; Wang, F.; Eidson, N.; Fan, X.; Han, F.; Luo, C.; Mao, M.; Li, X.; Wang, C. Existence of Solid Electrolyte Interphase in Mg Batteries: Mg/S Chemistry as an Example. *ACS Appl. Mater. Interfaces* **2018**, *10*, 14767−14776.
(10) Shterenberg, I.; Salama, M.; Gofer, Y.; Levi, E.; Aurbach, D. The challenge of developing rechargeable magnesium batteries. *MRS Bull.* **2014**, *39*, 453−460.
(11) Aurbach, D.; Gizbar, H.; Schechter, A.; Chusid, O.; Gottlieb, H. E.; Gofer, Y.; Goldberg, I. Electrolyte Solutions for Rechargeable Magnesium Batteries Based on Organomagnesium Chloroaluminate Complexes. *J. Electrochem. Soc.* **2002**, *149*, A115−A121.
(12) Aurbach, D.; Suresh, G. S.; Levi, E.; Mitelman, A.; Mizrahi, O.; Chusid, O.; Brunelli, M. Progress in Rechargeable Magnesium Battery Technology. *Adv. Mater.* **2007**, *19*, 4260−4267.
(13) Emly, A.; Van der Ven, A. Mg Intercalation in Layered and Spinel Host Crystal Structures for Mg Batteries. *Inorg. Chem.* **2015**, *54*, 4394−4402.
(14) Yoo, H. D.; Liang, Y.; Dong, H.; Lin, J.; Wang, H.; Liu, Y.; Ma, L.; Wu, T.; Li, Y.; Ru, Q.; Jing, Y.; An, Q.; Zhou, W.; Guo, J.; Lu, J.; Pantelides, S. T.; Qian, X.; Yao, Y. Fast kinetics of magnesium monochloride cations in interlayer-expanded titanium disulfide for magnesium rechargeable batteries. *Nat. Commun.* **2017**, *8*, No. 339.
(15) Whittingham, M. S. Electrical Energy Storage and Intercalation Chemistry. *Science* **1976**, *192*, 1126−1127.
(16) Holleck, G. L.; Driscoll, J. R. Transition metal sulfides as cathodes for secondary lithium batteries—II. titanium sulfides. *Electrochim. Acta* **1977**, *22*, 647−655.
(17) Mizushima, K.; Jones, P. C.; Wiseman, P. J.; Goodenough, J. B. Li_xCoO_2 ($0 < x < -1$): A new cathode material for batteries of high energy density. *Mater. Res. Bull.* **1980**, *15*, 783−789.
(18) Ozawa, K. Lithium-ion rechargeable batteries with $LiCoO_2$ and carbon electrodes: the $LiCoO_2$/C system. *Solid State Ionics* **1994**, *69*, 212−221.
(19) Liu, M.; Jain, A.; Rong, Z.; Qu, X.; Canepa, P.; Malik, R.; Ceder, G.; Persson, K. A. Evaluation of sulfur spinel compounds for multivalent battery cathode applications. *Energy Environ. Sci.* **2016**, *9*, 3201−3209.
(20) Liu, M.; Rong, Z.; Malik, R.; Canepa, P.; Jain, A.; Ceder, G.; Persson, K. A. Spinel compounds as multivalent battery cathodes: a systematic evaluation based on ab initio calculations. *Energy Environ. Sci.* **2015**, *8*, 964−974.
(21) Bucur, C. B.; Gregory, T.; Oliver, A. G.; Muldoon, J. Confession of a Magnesium Battery. *J. Phys. Chem. Lett.* **2015**, *6*, 3578−3591.
(22) Huie, M. M.; Bock, D. C.; Takeuchi, E. S.; Marschilok, A. C.; Takeuchi, K. J. Cathode materials for magnesium and magnesium-ion based batteries. *Coord. Chem. Rev.* **2015**, *287*, 15−27.
(23) Rong, Z.; Malik, R.; Canepa, P.; Sai Gautam, G.; Liu, M.; Jain, A.; Persson, K.; Ceder, G. Materials Design Rules for Multivalent Ion Mobility in Intercalation Structures. *Chem. Mater.* **2015**, *27*, 6016−6021.
(24) Aydinol, M. K.; Kohan, A. F.; Ceder, G. Ab initio calculation of the intercalation voltage of lithium-transition-metal oxide electrodes for rechargeable batteries. *J. Power Sources* **1997**, *68*, 664−668.
(25) Levi, M. D.; Lancri, E.; Levi, E.; Gizbar, H.; Gofer, Y.; Aurbach, D. The effect of the anionic framework of Mo_6X_8 Chevrel Phase (X = S, Se) on the thermodynamics and the kinetics of the electrochemical insertion of Mg^{2+} ions. *Solid State Ionics* **2005**, *176*, 1695−1699.
(26) Levi, E.; Levi, M. D.; Chasid, O.; Aurbach, D. A review on the problems of the solid state ions diffusion in cathodes for rechargeable Mg batteries. *J. Electroceram.* **2009**, *22*, 13−19.
(27) Suresh, G. S.; Levi, M. D.; Aurbach, D. Effect of chalcogen substitution in mixed $Mo_6S_{8-n}Se_n$ (n = 0, 1, 2) Chevrel phases on the thermodynamics and kinetics of reversible Mg ions insertion. *Electrochim. Acta* **2008**, *53*, 3889−3896.
(28) Tarascon, J. M.; Disalvo, F. J.; Murphy, D. W.; Hull, G. W.; Rietman, E. A.; Waszczak, J. V. Stoichiometry and physical properties of ternary molybdenum chalcogenides $M_xMo_6X_8$ (X = S, Se; M = Li, Sn, Pb). *J. Solid State Chem.* **1984**, *54*, 204−212.
(29) Cabello, M.; Alcántara, R.; Nacimiento, F.; Ortiz, G.; Lavela, P.; Tirado, J. L. Electrochemical and chemical insertion/deinsertion of magnesium in spinel-type $MgMn_2O_4$ and lambda-MnO_2 for both aqueous and non-aqueous magnesium-ion batteries. *CrystEngComm* **2015**, *17*, 8728−8735.
(30) Truong, Q. D.; Kempaiah Devaraju, M.; Tran, P. D.; Gambe, Y.; Nayuki, K.; Sasaki, Y.; Honma, I. Unravelling the Surface Structure of $MgMn_2O_4$ Cathode Materials for Rechargeable Magnesium-Ion Battery. *Chem. Mater.* **2017**, *29*, 6245−6251.
(31) Gu, Y.; Katsura, Y.; Yoshino, T.; Takagi, H.; Taniguchi, K. Rechargeable magnesium-ion battery based on a $TiSe_2$-cathode with d-p orbital hybridized electronic structure. *Sci. Rep.* **2015**, *5*, No. 12486.
(32) Kouji, T.; Yunpeng, G.; Yukari, K.; Takafumi, Y.; Hidenori, T. Rechargeable Mg battery cathode TiS_3 with d−p orbital hybridized electronic structures. *Appl. Phys. Express* **2016**, *9*, No. 011801.
(33) Sun, X.; Bonnick, P.; Nazar, L. F. Layered TiS_2 Positive Electrode for Mg Batteries. *ACS Energy Lett.* **2016**, *1*, 297−301.
(34) Dambournet, D.; Belharouak, I.; Amine, K. Tailored Preparation Methods of TiO_2 Anatase, Rutile, Brookite: Mechanism of Formation and Electrochemical Properties. *Chem. Mater.* **2010**, *22*, 1173−1179.
(35) Gui, Z.; Fan, R.; Mo, W.; Chen, X.; Yang, L.; Zhang, S.; Hu, Y.; Wang, Z.; Fan, W. Precursor Morphology Controlled Formation of Rutile VO_2 Nanorods and Their Self-Assembled Structure. *Chem. Mater.* **2002**, *14*, 5053−5056.
(36) McKelvy, M. J.; Glaunsinger, W. S. Synthesis and characterization of nearly stoichiometric titanium disulfide. *J. Solid State Chem.* **1987**, *66*, 181−188.
(37) Joe, Y. I.; Chen, X. M.; Ghaemi, P.; Finkelstein, K. D.; de la Peña, G. A.; Gan, Y.; Lee, J. C. T.; Yuan, S.; Geck, J.; MacDougall, G. J.; Chiang, T. C.; Cooper, S. L.; Fradkin, E.; Abbamonte, P. Emergence of charge density wave domain walls above the superconducting dome in 1T-$TiSe_2$. *Nat. Phys.* **2014**, *10*, 421−425.
(38) Thompson, A. H.; Scanlon, J. C.; Symon, C. R. The electrochemical reaction of Li with VSe_2 and implications on the ionicity of intercalation compounds. *Solid State Ionics* **1980**, *1*, 47−57.
(39) Pan, H.; Mengyu, Y.; Guobin, Z.; Ruimin, S.; Lineng, C.; Qinyou, A.; Liqiang, M. Layered VS_2 Nanosheet-Based Aqueous Zn Ion Battery Cathode. *Adv. Energy Mater.* **2017**, *7*, No. 1601920.
(40) Ōnuki, Y.; Rumiko, I.; Sei-ich, T.; Shōji, Y.; Hiroshi, K. Electrochemical Characteristics of TiS_2, $ZrSe_2$ and VSe_2 in Secondary Lithium Battery. *Jpn. J. Appl. Phys.* **1981**, *20*, 1583−1588.
(41) Dines, M. B. Lithium intercalation via n-Butyllithium of the layered transition metal dichalcogenides. *Mater. Res. Bull.* **1975**, *10*, 287−291.
(42) Thompson, A. H. Pauling's Ionicity and Charge-Density Waves in Layered Transition-Metal Dichalcogenides. *Phys. Rev. Lett.* **1975**, *34*, 520−524.
(43) Thompson, A. H.; Silbernagel, B. G. Correlated magnetic and transport properties in the charge-density-wave states of VSe_2. *Phys. Rev. B* **1979**, *19*, 3420−3426.
(44) Zhu, Y.; Xu, Y.; Liu, Y.; Luo, C.; Wang, C. Comparison of electrochemical performances of olivine $NaFePO_4$ in sodium-ion batteries and olivine $LiFePO_4$ in lithium-ion batteries. *Nanoscale* **2013**, *5*, 780−787.
(45) Weppner, W.; Huggins, R. A. Determination of the Kinetic Parameters of Mixed-Conducting Electrodes and Application to the System Li_3Sb. *J. Electrochem. Soc.* **1977**, *124*, 1569−1578.
(46) Fan, X.; Zhu, Y.; Luo, C.; Suo, L.; Lin, Y.; Gao, T.; Xu, K.; Wang, C. Pomegranate-Structured Conversion-Reaction Cathode with a Built-in Li Source for High-Energy Li-Ion Batteries. *ACS Nano* **2016**, *10*, 5567−5577.
(47) Wen, C. J.; Boukamp, B. A.; Huggins, R. A.; Weppner, W. Thermodynamic and Mass Transport Properties of "LiAl". *J. Electrochem. Soc.* **1979**, *126*, 2258−2266.
(48) Levi, M. D.; Gofer, Y.; Cherkinsky, M.; Birsa, M. L.; Aurbach, D.; Berlin, A. Electroanalytical features of non-uniformly doped

DOI: 10.1021/acs.chemmater.8b05218
Chem. Mater. 2019, 31, 3183−3191

conducting poly-3-(3,4,5-trifluorophenyl)thiophene films. *Phys. Chem. Chem. Phys.* **2003**, *5*, 2886−2893.
(49) Lindström, H.; Södergren, S.; Solbrand, A.; Rensmo, H.; Hjelm, J.; Hagfeldt, A.; Lindquist, S.-E. Li^+ Ion Insertion in TiO_2 (Anatase). 2. Voltammetry on Nanoporous Films. *J. Phys. Chem. B* **1997**, *101*, 7717−7722.
(50) Bard, A. J.; Faulkner, L. R.; Leddy, J.; Zoski, C. G. *Electrochemical Methods: Fundamentals and Applications*; Wiley: New York, 1980; Vol. *2*.
(51) Kim, H.-S.; Cook, J. B.; Lin, H.; Ko, J. S.; Tolbert, S. H.; Ozolins, V.; Dunn, B. Oxygen vacancies enhance pseudocapacitive charge storage properties of MoO_{3-x}. *Nat. Mater.* **2017**, *16*, 454−460.
(52) Augustyn, V.; Come, J.; Lowe, M. A.; Kim, J. W.; Taberna, P.-L.; Tolbert, S. H.; Abruña, H. D.; Simon, P.; Dunn, B. High-rate electrochemical energy storage through Li^+ intercalation pseudocapacitance. *Nat. Mater.* **2013**, *12*, 518−522.
(53) Ge, P.; Zhang, C.; Hou, H.; Wu, B.; Zhou, L.; Li, S.; Wu, T.; Hu, J.; Mai, L.; Ji, X. Anions induced evolution of Co_3X_4 (X = O, S, Se) as sodium-ion anodes: The influences of electronic structure, morphology, electrochemical property. *Nano Energy* **2018**, *48*, 617−629.
(54) Thöle, F.; Wan, L. F.; Prendergast, D. Re-examining the Chevrel phase Mo_6S_8 cathode for Mg intercalation from an electronic structure perspective. *Phys. Chem. Chem. Phys.* **2015**, *17*, 22548−22551.
(55) Pan, H. Electronic and Magnetic Properties of Vanadium Dichalcogenides Monolayers Tuned by Hydrogenation. *J. Phys. Chem. C* **2014**, *118*, 13248−13253.
(56) Zhang, Y.; Wu, X. Vanadium sulfide nanoribbons: Electronic and magnetic properties. *Phys. Lett. A* **2013**, *377*, 3154−3157.
(57) Zhang, Z.; Niu, J.; Yang, P.; Gong, Y.; Ji, Q.; Shi, J.; Fang, Q.; Jiang, S.; Li, H.; Zhou, X.; Gu, L.; Wu, X.; Zhang, Y. Van der Waals Epitaxial Growth of 2D Metallic Vanadium Diselenide Single Crystals and their Extra-High Electrical Conductivity. *Adv. Mater.* **2017**, *29*, No. 1702359.
(58) Cucinotta, C. S.; Dolui, K.; Pettersson, H.; Ramasse, Q. M.; Long, E.; O'Brian, S. E.; Nicolosi, V.; Sanvito, S. Electronic Properties and Chemical Reactivity of TiS_2 Nanoflakes. *J. Phys. Chem. C* **2015**, *119*, 15707−15715.
(59) Bonnick, P.; Blanc, L.; Vajargah, S. H.; Lee, C.-W.; Sun, X.; Balasubramanian, M.; Nazar, L. F. Insights into Mg^{2+} Intercalation in a Zero-Strain Material: Thiospinel $Mg_xZr_2S_4$. *Chem. Mater.* **2018**, *30*, 4683−4693.
(60) Sun, X.; Bonnick, P.; Duffort, V.; Liu, M.; Rong, Z.; Persson, K. A.; Ceder, G.; Nazar, L. F. A high capacity thiospinel cathode for Mg batteries. *Energy Environ. Sci.* **2016**, *9*, 2273−2277.
(61) Truong, Q. D.; Devaraju, M. K.; Honma, I. Nanocrystalline $MgMnSiO_4$ and $MgCoSiO_4$ particles for rechargeable Mg-ion batteries. *J. Power Sources* **2017**, *361*, 195−202.
(62) Orikasa, Y.; Masese, T.; Koyama, Y.; Mori, T.; Hattori, M.; Yamamoto, K.; Okado, T.; Huang, Z.-D.; Minato, T.; Tassel, C.; Kim, J.; Kobayashi, Y.; Abe, T.; Kageyama, H.; Uchimoto, Y. High energy density rechargeable magnesium battery using earth-abundant and non-toxic elements. *Sci. Rep.* **2014**, *4*, No. 5622.
(63) Aurbach, D.; Lu, Z.; Schechter, A.; Gofer, Y.; Gizbar, H.; Turgeman, R.; Cohen, Y.; Moshkovich, M.; Levi, E. Prototype systems for rechargeable magnesium batteries. *Nature* **2000**, *407*, 724−727.
(64) Ling, C.; Suto, K. Thermodynamic origin of irreversible magnesium trapping in chevrel phase Mo_6S_8: importance of magnesium and vacancy ordering. *Chem. Mater.* **2017**, *29*, 3731−3739.
(65) Heath, J.; Chen, H.; Islam, M. S. $MgFeSiO_4$ as a potential cathode material for magnesium batteries: ion diffusion rates and voltage trends. *J. Mater. Chem. A* **2017**, *5*, 13161−13167.
(66) Zhang, R.; Ling, C. Unveil the Chemistry of Olivine $FePO_4$ as Magnesium Battery Cathode. *ACS Appl. Mater. Interfaces* **2016**, *8*, 18018−18026.
(67) Li, X.-L.; Li, Y.-D. MoS_2 Nanostructures: Synthesis and Electrochemical Mg^{2+} Intercalation. *J. Phys. Chem. B* **2004**, *108*, 13893−13900.
(68) Liu, Y.; Jiao, L.; Wu, Q.; Du, J.; Zhao, Y.; Si, Y.; Wang, Y.; Yuan, H. Sandwich-structured graphene-like MoS_2/C microspheres for rechargeable Mg batteries. *J. Mater. Chem. A* **2013**, *1*, 5822−5826.
(69) Yagi, S.; Fukuda, M.; Ichitsubo, T.; Nitta, K.; Mizumaki, M.; Matsubara, E. EQCM Analysis of Redox Behavior of CuFe Prussian Blue Analog in Mg Battery Electrolytes. *J. Electrochem. Soc.* **2015**, *162*, A2356−A2361.
(70) Lipson, A. L.; Han, S.-D.; Kim, S.; Pan, B.; Sa, N.; Liao, C.; Fister, T. T.; Burrell, A. K.; Vaughey, J. T.; Ingram, B. J. Nickel hexacyanoferrate, a versatile intercalation host for divalent ions from nonaqueous electrolytes. *J. Power Sources* **2016**, *325*, 646−652.
(71) Wu, J.; Gao, G.; Wu, G.; Liu, B.; Yang, H.; Zhou, X.; Wang, J. $MgVPO_4F$ as a one-dimensional Mg-ion conductor for Mg ion battery positive electrode: a first principles calculation. *RSC Adv.* **2014**, *4*, 15014−15017.
(72) Kaveevivitchai, W.; Jacobson, A. J. High Capacity Rechargeable Magnesium-Ion Batteries Based on a Microporous Molybdenum−Vanadium Oxide Cathode. *Chem. Mater.* **2016**, *28*, 4593−4601.

DOI: 10.1021/acs.chemmater.8b05218
Chem. Mater. 2019, 31, 3183−3191